

Scalable *In Situ* Compression of Transient Simulation Data Using Time-Dependent Bases

Shaghayegh Zamani Ashtiani^a, Mujeeb R.Malik^b, Hessam Babae^a,

^a*Department of Mechanical Engineering, University of Pittsburgh, Pittsburgh, PA-15206.*

^b*NASA Langley Research Center, Hampton, VA-23681*

Abstract

Large-scale simulations of time-dependent problems generate a massive amount of data and with the explosive increase in computational resources the size of the data generated by these simulations has increased significantly. This has imposed severe limitations on the amount of data that can be stored and has elevated the issue of input/output (I/O) into one of the major bottlenecks of high-performance computing. In this work, we present an *in situ* compression technique to reduce the size of the data storage by orders of magnitude. This methodology is based on time-dependent subspaces and it extracts low-rank structures from multidimensional streaming data by decomposing the data into a set of time-dependent bases and a core tensor. We derive closed-form evolution equations for the core tensor as well as the time-dependent bases. The presented methodology does not require the data history and the computational cost of its extractions scales linearly with the size of data — making it suitable for large scale streaming datasets. To control the compression error, we present an adaptive strategy to add/remove modes to maintain the reconstruction error below a given threshold. We present four demonstration cases: (i) analytical example, (ii) incompressible unsteady reactive flow, (iii) stochastic turbulent reactive flow, and (iv) three-dimensional turbulent channel flow.

Keywords: Tensor decomposition, Real-time computation, Time-dependent bases, *in situ* compression

1. Introduction

The ability to perform large-scale simulations has grown explosively in the past few decades and it will only continue to grow in the near future. On the other hand, our ability to effectively analyze or in some applications even store the data that these simulations generate is lagging behind — impeding many scientific discoveries [1–3]. For extreme-scale simulations the sheer size of the data imposes input/output (I/O) constraints that impede storing temporally-resolved simulation data [4]. An example is the direct numerical simulation (DNS) of turbulent combustion, in which the creation of an ignition kernel – an intermittent phenomenon – occurs on the order of 10 simulation time steps, while typically every 400th time step is stored to maintain the I/O overhead at a reasonable level [5]. Similarly, climate simulations use time steps of minutes but model outputs are typically written at daily to monthly intervals, limiting the ability to understand extreme weather events and projections of their future changes. The I/O and network limitations motivate a paradigm shift from *postprocess-centric* to *concurrent* data analysis, wherein the raw data is analysed as it is generated in an *in situ* or *in-transit* framework and given the size of the data and the demand for real-time analysis, only scalable algorithms with low computational complexity have a chance of being feasible.

Being able to store time-dependent simulation data with higher temporal resolution is critically important for many purposes. One of the most common applications is checkpointing data for simulation restarts,

Email address: h.babae@pitt.edu (Hessam Babae)

where the simulation may need to restart from the last snapshot [6]. This is particularly important for parallel simulations with a large number of computational nodes with long runtimes, where node failure can interrupt the simulation or queue limits may be exceeded. Frequent checkpointing lowers the cost of loss in computational resources. The other applications are for data analysis, including visualization and extracting coherent structures from the simulation.

Data compression techniques can be broadly divided to *lossy* and *lossless* classes [7]. In the lossless compression, the compressed data has no error when compared to the decompressed data. Examples of lossless compression techniques are FPZIP [8] and ACE [9]. All of these techniques require a significant amount of memory and they are not suitable for large-scale simulations where only on-the-fly compression techniques are practical. On the other hand, lossy compression techniques can achieve significant reduction in data size by allowing controllable error in the reconstructed data. Lossy compression techniques can be further divided into methods that achieve compression by extracting and exploiting spatiotemporal correlations in the data and the methods that do not extract correlation. Examples of techniques that achieve compression by exploiting correlations in the data are methods based on low-rank matrix and tensor decompositions, for example QR decomposition [10], interpolated decomposition [11], singular value decomposition (SVD) [12, 13] or tensor decomposition based on higher order SVD (HOSVD) [14, 15]. Deep learning techniques that are based on autoencoder-decoder also achieve compression by extracting nonlinear correlations in the data [16–18]. Examples of the lossy compression techniques that do not exploit correlated structure in the data are multiprecision truncation methods [19], mesh reduction techniques that map the data to a coarse spatiotemporal mesh. See Ref. [17] for an overview of these techniques.

The focus of this work is on correlation-exploiting compression techniques as these lossy methods can achieve significantly more compression compared to other methods. The performance of these techniques can be assessed by two criteria: (i) the compression ratio for a given reconstruction error, and (ii) computational cost of performing the compression. The compression ratio is the ratio of the storage size of the full-dimensional data to that of the compressed data. Methods that can achieve higher compression ratio for a given accuracy or achieve higher accuracy for the same compression ratio perform better on the first metric. Computational cost of performing the compression of some techniques can be exceedingly large. For example, SVD-based reductions require solving large-scale eigenvalue problems and therefore, the computational cost of SVD-based compression can be orders of magnitudes larger than advancing the simulation for one time step – although this depends on the size of the data. This has motivated the randomized SVD that requires a single-pass over data [13], thereby reducing the computational cost significantly. To reduce the computational cost, deep-learning-based compression techniques can be trained on canonical problems and then the trained network can be used in real-time for fast compression [17]. However, it is not clear whether the pretrained model will perform well on any unseen data. This issue of extrapolating to unseen data does not exist in SVD-based techniques, as SVD reduction does not require any training, however, SVD-based techniques often result in lower compression ratios as they can only exploit linear correlations in data as opposed to autoencoder-decoder techniques that extract nonlinear correlations.

Recently, new reduced-order modeling techniques have been introduced in which the low-rank structures are extracted directly from the model – bypassing the need to generate data. In these techniques, a reduced-order model (ROM) is obtained by projecting the full-order model onto a time-dependent basis (TDB). We refer to these techniques as *model-driven* ROM, as opposed to *data-driven* techniques since in the model-driven formulation an evolution equation for TDB is derived. Model-driven ROMs have shown great performance in solving high-dimensional stochastic PDEs [20–25], reduced-order modeling of time-dependent linear systems [26–29]. TDB has also been applied in tensor dimension reduction with applications in quantum mechanics and quantum chemistry [30–33].

The attractive feature in model-driven techniques is that the low-rank subspace is time-dependent and it adapts to changes on the full order model. In this paper, we leverage that feature and present a data-

driven analog of the TDB-based compression. In particular, we present an adaptive and scalable *in situ* data compression that decomposes the streaming multidimensional data using TDBs. This technique extracts multidimensional correlations from high-dimensional streaming data. The presented method is lossy and it is adaptive, i.e., modes are added and removed to maintain the error below a prescribed threshold. Moreover, the method does not require the data history and it only utilizes the time derivative of the instantaneous data. As a result, the compression is achieved without having to solve large-scale eigenvalue or nonconvex optimization problems. The cost of extracting the data-driven TDB grows linearly with the data size, making it suitable for large-scale simulations where only on-the-fly compression techniques are feasible. We also present our formulation in a versatile form, where the multidimensional data can be decomposed into arbitrarily chosen lower-dimensional bases. In this new formulation, we recover the dynamically bi-orthonormal (DBO) decomposition [25], and equivalently, the dynamically orthogonal (DO) and bi-orthogonal (BO) [20, 21] decompositions as special cases. After introducing our strategy in the section 2, we test our method on four different compression problems, including the Runge function, incompressible turbulent reactive flow, stochastic turbulent reactive flow, and three-dimensional turbulent channel flow in section 3. In section 4, we summarize our work and suggest possible future work..

2. Methodology

2.1. Notations and Definitions

We consider that streaming data are generated by a generic d -dimensional nonlinear time-dependent PDE expressed by:

$$\frac{\partial v(\mathbf{x}, t)}{\partial t} = \mathcal{M}(v, \mathbf{x}, t), \quad \mathbf{x} \in \Omega, \quad t > 0, \quad (2.1)$$

where $\mathbf{x} = \{x_1, x_2, \dots, x_d\}$ are the d -dimensional independent variables, which include *differential* dimensions with respect to which differentiation appears in the PDE as well as *parametric/random* dimensions to which the solution of the PDE has parametric dependence. The examples of the parametric space are design space or random parametric space, where different samples of parameters can be run concurrently. In Eq. 2.1, \mathcal{M} represents the model that in general includes linear and nonlinear differential operators augmented with appropriate boundary/initial conditions. In the most generic form, we consider a disjoint decomposition of \mathbf{x} into p groups of variables: $\mathbf{x} = \{\mathbf{x}_1, \mathbf{x}_2, \dots, \mathbf{x}_p\}$, with $2 \leq p \leq d$. The dimension of each space \mathbf{x}_n is denoted by d_n . Therefore, $d = d_1 + d_2 + \dots + d_p$ and the special case of $p = d$ implies decomposing the d -dimensional space to d one-dimensional spaces.

In the presented methodology, we work with data, which is represented in the discrete form with vectors, matrices and tensors. However, we present our formulation using multidimensional functions, i.e., in the continuous form, since we believe this notation is easier to understand. We show how the continuous formulation can easily be turned to a discrete formulation.

We introduce an L^2 inner-product and its induced norm for the multidimensional space as in the following

$$\langle u(\mathbf{x}), v(\mathbf{x}) \rangle_{\mathbf{x}} := \int_{\mathbf{x}_p} \dots \int_{\mathbf{x}_1} u(\mathbf{x})v(\mathbf{x})\rho(\mathbf{x}_1) \dots \rho(\mathbf{x}_p)d\mathbf{x}_1 \dots d\mathbf{x}_p \quad \text{and} \quad \|u\|_{\mathbf{x}} := \langle u, u \rangle_{\mathbf{x}}^{\frac{1}{2}}, \quad (2.2)$$

where $\rho(\mathbf{x}_i)$ is the nonnegative density weight in each space. Similarly, an inner product for \mathbf{x}_n and its induced L^2 norm can be defined as:

$$\langle u(\mathbf{x}_n), v(\mathbf{x}_n) \rangle_{\mathbf{x}_n} = \int_{\mathbf{x}_n} u(\mathbf{x}_n)v(\mathbf{x}_n)\rho(\mathbf{x}_n)d\mathbf{x}_n, \quad \text{and} \quad \|u(\mathbf{x})\|_{\mathbf{x}_n} = \langle u(\mathbf{x}), u(\mathbf{x}) \rangle_{\mathbf{x}_n}^{\frac{1}{2}}. \quad (2.3)$$

We also introduce the following notation for the inner product with respect to all dimensions except \mathbf{x}_j as follows:

$$\langle u(\mathbf{x}, t), v(\mathbf{x}, t) \rangle_{\mathbf{x} \setminus \mathbf{x}_j} = \int_{\mathbf{x}_p} \dots \int_{\mathbf{x}_{j+1}} \int_{\mathbf{x}_{j-1}} \dots \int_{\mathbf{x}_1} u(\mathbf{x}, t)v(\mathbf{x}, t)\rho(\mathbf{x}_1) \dots \rho(\mathbf{x}_{j-1})\rho(\mathbf{x}_{j+1}) \dots \rho(\mathbf{x}_p)d\mathbf{x}_1 \dots d\mathbf{x}_{j-1}d\mathbf{x}_{j+1} \dots d\mathbf{x}_p. \quad (2.4)$$

We also denote a set of orthonormal time-dependent bases (TDB) in space \mathbf{x}_n by:

$$\mathbf{U}^{(n)}(\mathbf{x}_n, t) = [u_1^{(n)}(\mathbf{x}_n, t)|u_2^{(n)}(\mathbf{x}_n, t)|\dots|u_{r_n}^{(n)}(\mathbf{x}_n, t)],$$

where the superscript (n) shows the index of the dimension group and r_n is the dimension of the subspace spanned by $\mathbf{U}^{(n)}(\mathbf{x}_n, t)$. We also use the tensor notation that was presented in the review article [34]. For a t -order tensor $\underline{\mathbf{T}} \in \mathbb{R}^{r_1 \times r_2 \times \dots \times r_p}$, the n th or n -mode unfolding of a tensor to a matrix is denoted by: $\underline{\mathbf{T}}_{(n)}(t) \in \mathbb{R}^{r_n \times r_{n+1} \times \dots \times r_p r_1 r_2 \dots r_{n-1}}$. The n -mode product of $\underline{\mathbf{T}} \in \mathbb{R}^{r_1 \times r_2 \times \dots \times r_p}$ and the matrix $\mathbf{A} \in \mathbb{R}^{N_n \times r_n}$ is defined as $\underline{\mathbf{T}} \times_n \mathbf{A} \in \mathbb{R}^{r_1 \times r_2 \times \dots \times r_{n-1} \times N_n \times r_{n+1} \times \dots \times r_p}$. We also denote the time derivative with $\partial(\sim)/\partial t \equiv \dot{(\sim)}$.

2.2. Reduction via Time-dependent Bases

We decompose the multidimensional streaming data into a time-dependent core tensor and a set of time-dependent orthonormal TDB as in the following:

$$v(\mathbf{x}, t) = \sum_{i_p=1}^{r_p} \dots \sum_{i_2=1}^{r_2} \sum_{i_1=1}^{r_1} \underline{\mathbf{T}}_{i_1 i_2 \dots i_p}(t) u_{i_1}^{(1)}(\mathbf{x}_1, t) u_{i_2}^{(2)}(\mathbf{x}_2, t) \dots u_{i_p}^{(p)}(\mathbf{x}_p, t) + e(\mathbf{x}, t), \quad (2.5)$$

where $\underline{\mathbf{T}}(t)$ is the time-dependent core tensor and $\mathbf{U}^{(n)}(\mathbf{x}_n, t) = [u_1^{(n)}(\mathbf{x}_n, t)|u_2^{(n)}(\mathbf{x}_n, t)|\dots|u_{r_n}^{(n)}(\mathbf{x}_n, t)]$ are a set of orthonormal modes and $e(\mathbf{x}, t)$ is the low-rank approximation error. In the above description, $v(\mathbf{x}, t)$ represents the streaming data, which in the discrete form is represented by a d -dimensional time-dependent tensor. In the following, we derive closed-form evolution equations for the core tensor and the TDB. For the sake of simplicity, we derive the equations for a special case with three bases, where $p = 3$. We also present the formulation for the most generic case. The TDB is instantaneously orthonormal and therefore:

$$\langle u_i^{(n)}(\mathbf{x}_n, t), u_{i'}^{(n)}(\mathbf{x}_n, t) \rangle_{\mathbf{x}_n} = \delta_{ii'}, \quad i, i' = 1, 2, \dots, r_n, \quad n = 1, 2, \dots, p. \quad (2.6)$$

Taking time derivative of the orthonormality condition results in:

$$\frac{d}{dt} \langle u_i^{(n)}(\mathbf{x}_n, t), u_j^{(n)}(\mathbf{x}_n, t) \rangle_{\mathbf{x}_n} = \langle \dot{u}_i^{(n)}(\mathbf{x}_n, t), u_j^{(n)}(\mathbf{x}_n, t) \rangle_{\mathbf{x}_n} + \langle u_i^{(n)}(\mathbf{x}_n, t), \dot{u}_j^{(n)}(\mathbf{x}_n, t) \rangle_{\mathbf{x}_n} = 0. \quad (2.7)$$

Let $\phi_{ij}^{(n)}(t) = \langle \dot{u}_i^{(n)}(\mathbf{x}_n, t), u_j^{(n)}(\mathbf{x}_n, t) \rangle_{\mathbf{x}_n}$, where $\phi_{ij}^{(n)}(t) \in \mathbb{R}^{r_n \times r_n}$. From Eq. 2.7, it is clear that $\phi_{ij}^{(n)}(t)$ is a skew-symmetric matrix $\phi_{ij}^{(n)}(t) = -\phi_{ij}^{(n)T}(t)$. Based on the above definitions, we derive the evolution equations for the bases and the core tensor. To this end, we take a time derivative of the TDB decomposition given by Eq. 2.5. This follows:

$$\dot{v} = \dot{\underline{\mathbf{T}}}_{i_1 i_2 i_3} u_{i_1}^{(1)} u_{i_2}^{(2)} u_{i_3}^{(3)} + \underline{\mathbf{T}}_{i_1 i_2 i_3} \dot{u}_{i_1}^{(1)} u_{i_2}^{(2)} u_{i_3}^{(3)} + \underline{\mathbf{T}}_{i_1 i_2 i_3} u_{i_1}^{(1)} \dot{u}_{i_2}^{(2)} u_{i_3}^{(3)} + \underline{\mathbf{T}}_{i_1 i_2 i_3} u_{i_1}^{(1)} u_{i_2}^{(2)} \dot{u}_{i_3}^{(3)}. \quad (2.8)$$

By taking the inner product $\langle \bullet, u_{i_1}^{(1)} u_{i_2}^{(2)} u_{i_3}^{(3)} \rangle_{\mathbf{x}}$ of Eq. 2.8 and using orthonormality conditions, the evolution of the core tensor is obtained as follows:

$$\dot{\underline{\mathbf{T}}}_{i_1' i_2' i_3'} = \langle \dot{v}, u_{i_1'}^{(1)} u_{i_2'}^{(2)} u_{i_3'}^{(3)} \rangle_{\mathbf{x}} - \underline{\mathbf{T}}_{i_1 i_2' i_3'} \phi_{i_1' i_1}^{(1)} - \underline{\mathbf{T}}_{i_1' i_2 i_3} \phi_{i_2' i_2}^{(2)} - \underline{\mathbf{T}}_{i_1' i_2' i_3} \phi_{i_3' i_3}^{(3)}. \quad (2.9)$$

To derive the evolution equation for the bases, we start with deriving an expression for $\dot{u}_{i_1}^{(1)}$ by taking the inner product $\langle \bullet, u_{i_2}^{(2)} u_{i_3}^{(3)} \rangle_{\mathbf{x} \setminus \mathbf{x}_1}$ of Eq. 2.8 as follows:

$$\langle \dot{v}, u_{i_2}^{(2)} u_{i_3}^{(3)} \rangle_{\mathbf{x} \setminus \mathbf{x}_1} = \dot{\underline{\mathbf{T}}}_{i_1 i_2' i_3'} u_{i_1}^{(1)} + \underline{\mathbf{T}}_{i_1 i_2' i_3'} \dot{u}_{i_1}^{(1)} + \underline{\mathbf{T}}_{i_1 i_2 i_3'} u_{i_1}^{(1)} \phi_{i_2' i_2}^{(2)} + \underline{\mathbf{T}}_{i_1 i_2 i_3} u_{i_1}^{(1)} \phi_{i_3' i_3}^{(3)}. \quad (2.10)$$

By rearranging the indexes for $\dot{\underline{\mathbf{T}}}_{i_1' i_2' i_3'}$ from Eq. 2.9:

$$\dot{\underline{\mathbf{T}}}_{i_1' i_2' i_3'} = \langle \dot{v}, u_{i_1}^{(1)} u_{i_2}^{(2)} u_{i_3}^{(3)} \rangle_{\mathbf{x}} - \underline{\mathbf{T}}_{j_1 i_2' i_3'} \phi_{i_1' j_1}^{(1)} - \underline{\mathbf{T}}_{i_1' i_2 i_3} \phi_{i_2' i_2}^{(2)} - \underline{\mathbf{T}}_{i_1' i_2 i_3} \phi_{i_3' i_3}^{(3)}.$$

We can substitute it into Eq. 2.10 and derive the evolution equation for the first bases:

$$\underline{\mathbf{T}}_{i_1 i_2' i_3'} \dot{u}_{i_1}^{(1)} = \langle \dot{v}, u_{i_2}^{(2)} u_{i_3'}^{(3)} \rangle_{\mathbf{x} \setminus \mathbf{x}_1} - u_{i_1}^{(1)} [\langle \dot{v}, u_{i_1}^{(1)} u_{i_2}^{(2)} u_{i_3'}^{(3)} \rangle_{\mathbf{x}} - \underline{\mathbf{T}}_{j_1 i_2' i_3'} \phi_{i_1 j_1}^{(1)}]. \quad (2.11)$$

We denote the orthogonal projection onto the complement space spanned by $\mathbf{U}^{(1)}$ as in the following:

$$\prod_{\mathbf{U}^{(1)}} \langle \dot{v}, u_{i_2}^{(2)} u_{i_3'}^{(3)} \rangle_{\mathbf{x} \setminus \mathbf{x}_1} = \langle \dot{v}, u_{i_2}^{(2)} u_{i_3'}^{(3)} \rangle_{\mathbf{x} \setminus \mathbf{x}_1} - \langle \langle \dot{v}, u_{i_2}^{(2)} u_{i_3'}^{(3)} \rangle_{\mathbf{x} \setminus \mathbf{x}_1}, u_{i_1}^{(1)} \rangle u_{i_1}^{(1)}.$$

Incorporating the above definition into Eq. 2.11 and rearranging the equation results in:

$$\underline{\mathbf{T}}_{i_1 i_2' i_3'} \dot{u}_{i_1}^{(1)} = \prod_{\mathbf{U}^{(1)}} \langle \dot{v}, u_{i_2}^{(2)} u_{i_3'}^{(3)} \rangle_{\mathbf{x} \setminus \mathbf{x}_1} + \underline{\mathbf{T}}_{i_1 i_2' i_3'} \phi_{i_1' i_1}^{(1)} u_{i_1}^{(1)}.$$

The above equation can be an underdetermined system with respect to unknowns $\dot{u}_{i_1}^{(1)}$ if $r_1 > r_2 r_3$ and it could be overdetermined otherwise. In order to address this issue, we find the least-square solution for $\dot{u}_{i_1}^{(1)}$. This can be accomplished by first multiplying both sides of the above equation by $\underline{\mathbf{T}}_{(1)}^T$ and then computing the inverse of the resulting matrix. This amounts to computing the pseudoinverse of the unfolded core tensor, which is denoted by $\mathbf{T}^{(1)\dagger}$. The resulting equation is:

$$\dot{u}_{i_1}^{(1)} = \prod_{\mathbf{U}^{(1)}} \langle \dot{v}, u_{i_2}^{(2)} u_{i_3'}^{(3)} \rangle_{\mathbf{x} \setminus \mathbf{x}_1} \mathbf{T}_{i_1, i_2' i_3'}^{(1)\dagger} + u_{i_1}^{(1)} \phi_{i_1' i_1}^{(1)}, \quad \mathbf{T}^{(1)\dagger} = \underline{\mathbf{T}}_{(1)}^T (\underline{\mathbf{T}}_{(1)} \underline{\mathbf{T}}_{(1)}^T)^{-1}, \quad \mathbf{T}_{i_1, i_2' i_3'}^{(1)\dagger} = \mathbf{T}_{i_1, i_2' + (i_3' - 1)r_2}^{(1)\dagger}.$$

In a similar manner, we can derive $\dot{u}_{i_2}^{(2)}$ and $\dot{u}_{i_3}^{(3)}$:

$$\dot{u}_{i_2}^{(2)} = \prod_{\mathbf{U}^{(2)}} \langle \dot{v}, u_{i_1}^{(1)} u_{i_3'}^{(3)} \rangle_{\mathbf{x} \setminus \mathbf{x}_2} \mathbf{T}_{i_2, i_1' i_3'}^{(2)\dagger} + u_{i_2}^{(2)} \phi_{i_2' i_2}^{(2)}, \quad \mathbf{T}^{(2)\dagger} = \underline{\mathbf{T}}_{(2)}^T (\underline{\mathbf{T}}_{(2)} \underline{\mathbf{T}}_{(2)}^T)^{-1}, \quad \mathbf{T}_{i_2, i_1' i_3'}^{(2)\dagger} = \mathbf{T}_{i_2, i_1' + (i_3' - 1)r_1}^{(2)\dagger},$$

$$\dot{u}_{i_3}^{(3)} = \prod_{\mathbf{U}^{(3)}} \langle \dot{v}, u_{i_1}^{(1)} u_{i_2}^{(2)} \rangle_{\mathbf{x} \setminus \mathbf{x}_3} \mathbf{T}_{i_3, i_1' i_2'}^{(3)\dagger} + u_{i_3}^{(3)} \phi_{i_3' i_3}^{(3)}, \quad \mathbf{T}^{(3)\dagger} = \underline{\mathbf{T}}_{(3)}^T (\underline{\mathbf{T}}_{(3)} \underline{\mathbf{T}}_{(3)}^T)^{-1}, \quad \mathbf{T}_{i_3, i_1' i_2'}^{(3)\dagger} = \mathbf{T}_{i_3, i_1' + (i_2' - 1)r_1}^{(3)\dagger}.$$

Similarly, we can derive the evolution equations for the general case where $2 \leq p \leq d$. To this end, we take the time derivative of Eq. 2.5 as follow:

$$\begin{aligned} \dot{v} &= \dot{\underline{\mathbf{T}}}_{i_1 i_2 \dots i_p} u_{i_1}^{(1)} u_{i_2}^{(2)} \dots u_{i_p}^{(p)} + \underline{\mathbf{T}}_{i_1 i_2 \dots i_p} \dot{u}_{i_1}^{(1)} u_{i_2}^{(2)} \dots u_{i_p}^{(p)} + \underline{\mathbf{T}}_{i_1 i_2 \dots i_p} u_{i_1}^{(1)} \dot{u}_{i_2}^{(2)} \dots u_{i_p}^{(p)} + \dots \\ &+ \underline{\mathbf{T}}_{i_1 i_2 \dots i_p} u_{i_1}^{(1)} u_{i_2}^{(2)} \dots \dot{u}_{i_p}^{(p)}. \end{aligned} \quad (2.12)$$

By taking the inner product $\langle \bullet, u_{i_1}^{(1)} u_{i_2}^{(2)} \dots u_{i_p}^{(p)} \rangle_{\mathbf{x}}$ of both sides of the Eq. 2.12 and using orthonormality conditions, the evolution of core tensor is obtained as follows:

$$\dot{\underline{\mathbf{T}}}_{i_1' i_2' \dots i_p'} = \langle \dot{v}, u_{i_1}^{(1)} u_{i_2}^{(2)} \dots u_{i_p}^{(p)} \rangle_{\mathbf{x}} - \underline{\mathbf{T}}_{i_1 i_2 \dots i_p} \phi_{i_1' i_1}^{(1)} - \underline{\mathbf{T}}_{i_1 i_2 \dots i_p} \phi_{i_2' i_2}^{(2)} - \dots - \underline{\mathbf{T}}_{i_1 i_2 \dots i_p} \phi_{i_p' i_p}^{(p)}. \quad (2.13)$$

To derive the evolution equation $\dot{u}_{i_j}(\mathbf{x}_j, t)$, we project both sides of Eq. 2.12 onto all bases except $u_{i_j}(\mathbf{x}_j, t)$. This can be accomplished by taking the inner product $\langle \bullet, u_{i_1}^{(1)} u_{i_2}^{(2)} \dots u_{i_{j-1}}^{(j-1)} u_{i_{j+1}}^{(j+1)} \dots u_{i_p}^{(p)} \rangle_{\mathbf{x} \setminus \mathbf{x}_j}$ of Eq. 2.12. Similar to the simplified derivation for $p = 3$, we substitute the evolution of the core tensor from Eq. 2.13 into our operations. This yields to:

$$\dot{u}_{i_j}^{(j)} = \prod_{\mathbf{U}^{(j)}} \langle \dot{v}, u_{i_1}^{(1)} u_{i_2}^{(2)} \dots u_{i_{j-1}}^{(j-1)} u_{i_{j+1}}^{(j+1)} \dots u_{i_p}^{(p)} \rangle_{\mathbf{x} \setminus \mathbf{x}_j} \mathbf{T}_{i_j, i_1' i_2' \dots i_{j-1}' i_{j+1}' \dots i_p'}^{(j)\dagger} + u_{i_j}^{(j)} \phi_{i_j' i_j}^{(j)}. \quad (2.14)$$

Here, any skew symmetric choice for ϕ results in an equivalent TDB approximation. For simplicity, we can choose it to be zero. Therefore, Eq. 2.13 and 2.14 would become as follow:

$$\dot{\underline{\mathbf{T}}}_{i_1' i_2' \dots i_p'} = \langle \dot{v}, u_{i_1}^{(1)} u_{i_2}^{(2)} \dots u_{i_p}^{(p)} \rangle_{\mathbf{x}}, \quad (2.15)$$

$$\dot{u}_{i_j}^{(j)} = \prod_{\mathbf{U}^{(j)}} \left\langle \dot{v}, u_{i_1}^{(1)} u_{i_2}^{(2)} \dots u_{i_{j-1}}^{(j-1)} u_{i_{j+1}}^{(j+1)} \dots u_{i_p}^{(p)} \right\rangle_{\mathbf{x} \setminus \mathbf{x}_j} \mathbf{T}_{i_j, i_1' i_2' \dots i_{j-1}' i_{j+1}' \dots i_p'}^{(j)\dagger} \quad (2.16)$$

Not only does the choice of $\phi = 0$ simplify the above evolution equation but also implies a simple interpretation where $u_{i_j}^{(j)}$ is always orthogonal to the space spanned by $u_{i_j}^{(j)}$ (dynamically orthogonal condition). This choice is also used for reduced-order modeling in Ref. [24, 25, 28, 35].

Equations 2.15 and 2.16 constitute the evolution equations for the TDB compression scheme. We note the DBO decomposition [25, 35] is a special case of the above scheme where $p = 2$. It has also been shown in Ref. [25] that DO and BO decompositions are equivalent to DBO, i.e., DO, BO and DBO extract the same subspace from the full-dimensional problem. In that sense, DO and BO are closely related to Eqs. 2.15 and 2.16 for the special case of $p = 2$. It is possible to derive data-driven evolution in the DO and BO forms. The data-driven formulation of the DO decomposition is presented in Ref. [24].

Equations 2.15 and 2.16 must be solved in the space-time discrete form and they must be augmented with appropriate initial conditions.

2.3. Time-Dependent Bases in Discrete Space-Time Form

In the previous section, we presented the TDB decomposition in the continuous space-time form. In this section, we show the details of how the above scheme can be applied to streaming data that are discrete in space and time. In the space-discrete form, the multidimensional data $(v(\mathbf{x}, t))$ are represented by a p -order time-dependent tensor denoted by: $\underline{\mathbf{V}}(t) \in \mathbb{R}^{N_1 \times N_2 \times \dots \times N_p}$. If data are generated by a simulation, N_1, N_2, \dots, N_p are the number of grid points. Note that the data may be generated by higher-dimensional independent variables, i.e., $d \geq p$. The orthonormal bases in the \mathbf{x}_n dimension can be represented as a time-dependent matrix: $\mathbf{U}^{(n)}(t) = [\mathbf{u}_1^{(n)}(t), \mathbf{u}_2^{(n)}(t), \dots, \mathbf{u}_{r_n}^{(n)}(t)] \in \mathbb{R}^{N_n \times r_n}$, where $\mathbf{u}_i^{(n)}$ is a discrete (vector) representation of u_i . We show the discrete form of the TDB formulation in figure 1 where the inner product in the space is approximated with a quadrature rule:

$$\langle u_i^{(n)}, u_j^{(n)} \rangle_{\mathbf{x}_n} \simeq \mathbf{u}_i^{(n)T} \mathbf{W}^{(n)} \mathbf{u}_j^{(n)}, \quad (2.17)$$

where $\mathbf{W}^{(n)} \in \mathbb{R}^{N_n \times N_n}$ is the diagonal matrix, whose diagonal elements are the quadrature weights. The time derivative of the streaming data ($\dot{\underline{\mathbf{V}}}(t)$) is computed with finite difference and the evolution equation for TDB and the core tensor can be advanced with a standard time-integration scheme. Various time discretization schemes can be used. High-order finite-difference discretizations require keeping the solution from multiple time steps in the memory. In the first demonstration example, we investigate the error introduced by using different temporal schemes for both $\dot{\underline{\mathbf{V}}}(t)$ and the evolution of TDB.

As we discuss in the next section, the TDB decomposition and the instantaneous HOSVD are closely connected. To this end, HOSVD of the full-dimensional data at $t = 0$ is used to initialize the core tensor as well as the TDB.

2.4. Extraction of Coherent Structure from Streaming Data

The TDB decomposition is closely related to the instantaneous HOSVD of the multidimensional data. The HOSVD extracts correlated structures for all p unfoldings of tensor $\underline{\mathbf{V}}(t)$. As we demonstrate in our examples, the HOSVD of the TDB core tensor $\underline{\mathbf{T}}(t)$ follows the leading singular values obtained by HOSVD of the full tensor $\underline{\mathbf{V}}(t)$. To establish the connection between HOSVD and TDB, let

$$\underline{\mathbf{T}}_{(n)}(t) = \mathbf{\Psi}^{(n)}(t) \mathbf{\Sigma}^{(n)}(t) \mathbf{\Theta}^{(n)T}(t), \quad (2.18)$$

be the SVD of the unfolded core tensor, where $\mathbf{\Sigma}^{(n)} = \text{diag}(\sigma_1^{(n)}, \dots, \sigma_{r_n}^{(n)})$ are the singular values of the n -mode unfolding of the core tensor, $\mathbf{\Psi}^{(n)}(t)$ and $\mathbf{\Theta}^{(n)}(t)$ are the left and right singular vectors of the unfolded core tensor. As we show in our demonstrations, $\mathbf{\Sigma}^{(n)}$ closely follows the r_n leading singular values of the n -mode unfolding of the full-dimensional streaming data ($\underline{\mathbf{V}}_{(n)}(t)$). Moreover, the TDB closely follows the

Figure 1: Time-dependent bases in discrete form. For simplicity weights are considered to be identity ($\mathbf{W}_{N_1 \times N_1}^{(1)} = \mathbf{I}$).

leading left singular vectors of $\underline{\mathbf{V}}_{(n)}(t)$ after rotating TDB along the energetically ranked direction by using $\Psi^{(n)}(t)$ as in the following:

$$\tilde{\mathbf{U}}^{(n)}(t) = \mathbf{U}^{(n)}(t) \Psi^{(n)}(t). \quad (2.19)$$

In other words, the TDB closely approximate the same subspace spanned by the leading left singular vectors of the the unfolded data. With the rotation given by Eq. 2.19, the TDB modes are ranked energetically and they can be compared against the left singular vectors of the the unfolded data. In the case of $p = 2$, where the high-dimensional data are matricized and TDB reduces to DBO, agreements between the TDB subspace and the instantaneously optimal subspace obtained from SVD of the full-dimensional data have already been established. See Ref. [25] for the case of stochastic reduced-order modeling, Ref. [35] for the case of reduced-order modeling of reactive species transport equation. This is also true for DO [36], OTD [37] and BO [38] formulations, which are all equivalent to the DBO formulation. In the case of linear dynamics, the convergence of TDB modes to the dominant subspace obtained by the SVD of the full-dimensional data is theoretically shown [37, 39].

The $\tilde{\mathbf{U}}^{(n)}(t)$ modes obtained from Eq. 2.19 captures the dominant structures among the columns of the n th unfolding of the full-dimensional data, and therefore, $\tilde{\mathbf{U}}^{(n)}(t)$ can be interpreted as instantaneous coherent structures in the streaming data.

2.5. Error Control and Adaptivity

For highly transient systems, the rank of the systems may change as the system evolves. Therefore, to maintain the error at a desirable level, the multirank (r_1, r_2, \dots, r_p) must change in time accordingly. There are two types of error in TDB decomposition: (i) temporal discretization error, and (ii) the error of the unresolved subspace, which are a result of neglecting the interactions of the resolved TDB subspace with the unresolved subspace. The lost interactions induce a *memory error* on TDB components that can be properly analyzed in the Mori-Zwanzig framework [40]. Unlike the model-driven TDB, in the data-driven mode, the error can be monitored by computing the Frobenius norm of the difference between the full data and TDB reconstruction, i.e.,

$$\varepsilon(t) = \|\underline{\mathbf{V}}(t) - \underline{\mathbf{V}}^{TDB}(t)\|_F. \quad (2.20)$$

The above Frobenius norm is defined based on the weighted inner product. To develop an adaptive strategy for TDB, we need to define an error criterion for mode addition/removal. Using singular values, we can

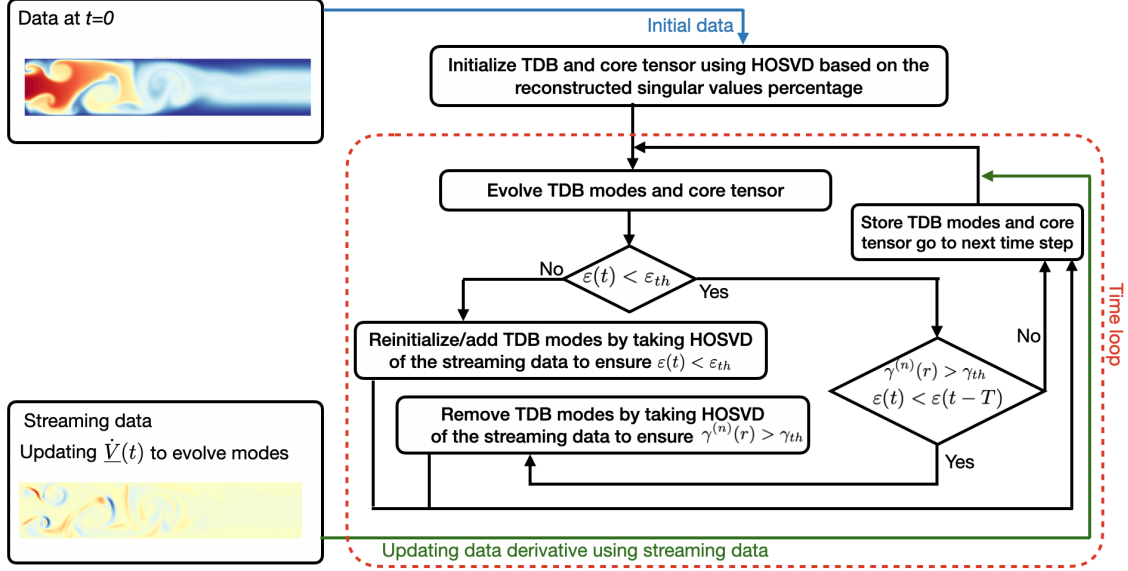


Figure 2: Algorithm flowchart for the compression and error adaptivity.

calculate the percentage of the captured detail as follow:

$$\gamma^{(n)}(r) = \frac{\sum_{i=1}^{r_n} \sigma_i^{(n)2}}{\sum_{i=1}^{N_n} \sigma_i^{(n)2}} \times 100 = \frac{\sum_{i=1}^{r_n} \sigma_i^{(n)2}}{\sum_{i=1}^{r_n} \sigma_i^{(n)2} + \varepsilon^2(t)} \times 100. \quad (2.21)$$

In order to control the error, we define a maximum allowable error for $\varepsilon(t)$, which is chosen by the practitioner. The adaptive algorithm adds modes if the error exceeds the threshold value and removes modes if the error can be maintained below the threshold with lower ranks based on the defined $\gamma^{(n)}(r)$. In particular, if the error exceeds the maximum error (ε_{th}), the algorithm: (i) reinitializes the core tensor and TDB; (ii) increases the number of modes if the resulting error from reinitialization stays above the limit; (iii) the algorithm reinitializes and reduces the number of modes if the solution starts to capture unnecessary energy and has a negative average slope for a defined number of iterations. In this process, we can increase/decrease the number of modes with respect to the relation between the defined error and singular values Eq. (2.21). For example, assume the maximum error limit is set to be $\varepsilon(t) = \varepsilon_{th}$. First, we initialize the TDB and the core tensor using HOSVD and calculate the required number of modes in each direction based on $\gamma^{(n)}(r) = \gamma_{th}$. During the computation, if $\varepsilon(t) > \varepsilon_{th}$, the algorithm reinitializes the modes. If the resulting error is not less than the prescribed limit, the algorithm increases the number of modes based on γ_{th} . In the subsequent time steps if $\gamma(t) > \gamma_{th}$, the algorithm decreases the number of modes. Note that, rank adjustment reinitializes the modes and the core tensor, which may reduce the error for only a few iterations. This causes frequent rank adjustment with high computational costs. Therefore, in addition to the defined error, the slope of the error for a defined number of iterations (excluding the time steps with HOSVD reinitialization) must be negative to trigger the rank reduction process. We show the algorithm of this example in figure 2.

2.6. Scalability and Compression Ratio

We show that the computational complexity of solving the resulting equations linearly scales with the size of the data. Here, for simplicity, we consider ($p = d$), i.e., one-dimensional TDB and $N = N_1 = N_2 = \dots = N_d$. In this case, the total size of the data is $S = N^d$. We also consider the case where the core tensor has equal n -ranks, i.e., $r = r_1 = r_2 = \dots = r_d$. The leading costs of evolving TDB equations are:

1. Projection of the time-derivative of the data onto TDB ($\mathbf{U}^{(n)T} \dot{\mathbf{V}}_{(n)}$), which is $\mathcal{O}(rdS)$.

2. Computing the pseudoinverse of the unfolded core tensor ($\mathbf{T}^{(n)\dagger}$). This requires the computation of $\underline{\mathbf{T}}_{(n)}\underline{\mathbf{T}}_{(n)}^T$, which scales with $\mathcal{O}(r^d)$ and the computation of the inverse of this matrix $(\underline{\mathbf{T}}_1\underline{\mathbf{T}}_1^T)^{-1}$, which scales with $\mathcal{O}(r^3)$.

We make the following observations about the cost of evolving TDB:

1. When $r \ll N$, the computational cost of computing the pseudoinverse of the unfolded core tensor is negligible to the projection of the time-derivative of the data onto TDB, which scales linearly with the total size of the data.
2. The evolution of TDB components does not require computation of any eigenvalue problem as required in SVD-based reductions or solving a nonlinear optimization problem as is required in autoencoder-decoder reductions [17, 41, 42].
3. Many entries of $\underline{\mathbf{V}}$ have small values. See figure 2 for an example of $\underline{\mathbf{V}}$. Therefore, the sparse approximation of $\underline{\mathbf{V}}$ can significantly reduce overall cost, although this advantage of TDB has not been explored in this work.

The computational cost of solving the TDB equations can be compared against that of computing HOSVD. HOSVD requires computing the SVDs of the unfolded tensor $\underline{\mathbf{V}}_{(n)}$ for $n = 1, 2, \dots, d$. This requires computation and storage of the correlation matrix $\mathbf{C}^{(n)} = \underline{\mathbf{V}}_{(n)}^T \underline{\mathbf{V}}_{(n)}$, which scales with $\mathcal{O}(dN^{d+1})$ and the eigenvalue computation of this matrix, which scales with N^3 . The computational cost of TDB and HOSVD for a block of data generated by the turbulent channel flow simulation (last demonstration) for the case of $N = N_1 = N_2 = N_3$ are shown in figure 3(a). This confirms that the computational cost of TDB scales linearly with the total data size $S = N^3$, while the computational cost of HOSVD scales with $N^3 = S^{4/3}$. This shows that TDB computations are significantly faster than HOSVD and the disparity between the computational cost of TDB and HOSVD only grows as the dimension or number of grid points (or samples) increases.

The compression ratio of the TDB decomposition is computed as the ratio of the storage cost of storing the full-dimensional data to that of solving the TDB components. The TDB requires storing the core tensor and the orthonormal lower-dimensional bases. Therefore, the compression ratio for TDB is:

$$CR = \frac{N_1 N_2 \dots N_p}{r_1 N_1 + r_2 N_2 + \dots + r_p N_p + r_1 r_2 \dots r_p}.$$

Figure 3(b) shows the compression ratio (CR) for the same problem with the corresponding error resulting from dimension reduction. Since our algorithm is adaptive, it can change the compression ratio by changing the number of modes; therefore, we introduce the weighted compression ratio \overline{CR} as follow:

$$\overline{CR} = \frac{t_m - t_0}{\frac{(t_1 - t_0)}{CR_1} + \frac{(t_2 - t_1)}{CR_2} \dots + \frac{(t_m - t_{m-1})}{CR_m}}. \quad (2.22)$$

Where, CR_1, CR_2, \dots, CR_m are compression ratios for $(t_1 - t_0), (t_2 - t_1), \dots, (t_m - t_{m-1})$ time intervals, respectively. This equation allows us to measure the effective compression ratio for all time intervals when the number of modes changes in adaptivity process.

3. Demonstration Cases

In this section, we present four demonstration cases for the application of TDB for the compression of streaming data: (i) Runge function; (ii) incompressible unsteady reactive flow; (iii) stochastic turbulent reactive flow, and (iv) three-dimensional turbulent channel flow.

3.1. Runge Function

We first demonstrate the adaptive TDB compression technique with one dimensional modes (i.e., $d = p$) for a time dependent Runge function as follow:

$$f(x_1, x_2, x_3, t) = \frac{1}{a(t)^2 + x_1^2 + x_2^2 + x_3^2}, \quad (3.1)$$

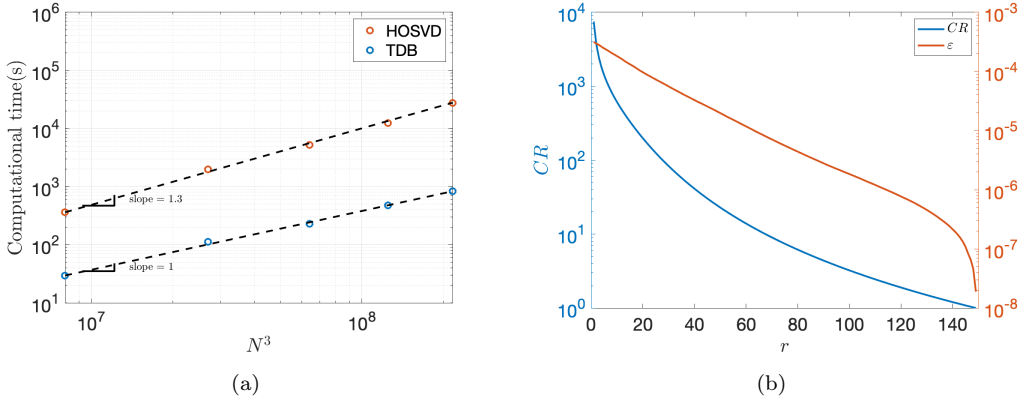


Figure 3: Computational performance for turbulent channel flow: (a) Scalability, (b) Compression ratio and resulting error.

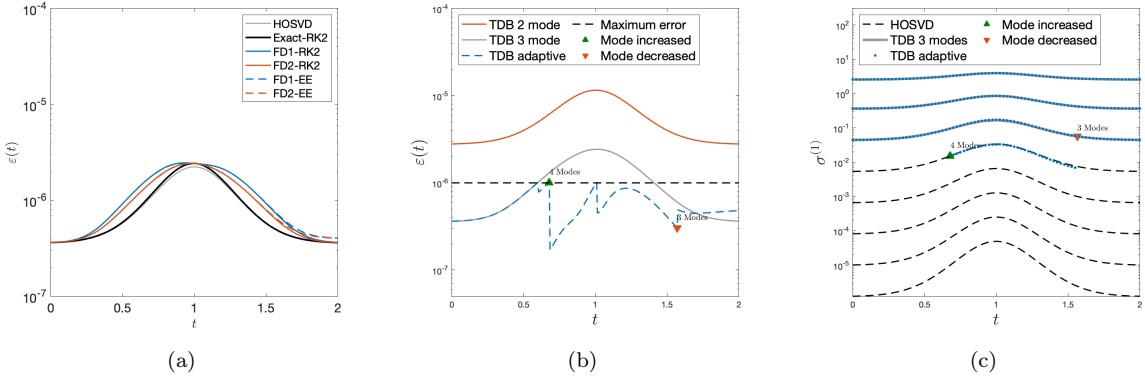


Figure 4: Runge function: (a) The effect of numerical and reduction error. (b) Comparing the effect of mode adjustment on error. (c) Singular values comparison.

where $a(t) = 1 - 0.5 \exp(-\alpha(t-1)^2)$ and $\alpha = 0.5$. For this choice of $a(t)$, the rank of the TDB decomposition must increase from $t = 0$ to $t = 1$ and then decrease to ensure that the low-rank approximation error remains below a specified value. The spatial domain is the cube $[-\pi, \pi]^3$ discretized on a uniform grid of size 126^3 . The time step $\Delta t = 5 \times 10^{-3}$ is used for evolving the TDB evolution equations.

In this problem, we use the same number of modes in each direction, i.e., $r = r_1 = r_2 = r_3$ due to the isotropy of function f . First, we show the effect of both unresolved and numerical errors in figure 4(a). Here, HOSVD error is the weighted Frobenius norm of the difference between reconstructed data from HOSVD and the streaming data, which shows the unresolved error from reduction. The implemented first-order Euler (EE) and second-order Runge-Kutta (RK) add numerical error to the existing unresolved error. The second-order RK scheme has less error and we use this scheme to show adaptivity effect. This figure also shows the error difference between the exact data derivative with its first-order, and central second-order approximation. In order to study the adaptivity procedure for this analytical problem, we used the data derivative instead of finite difference approximations. Figure 4(b) shows the reconstruction error versus time for fixed-rank TDB decompositions for $r = 2$ and $r = 3$ and adaptive TDB initiated with $r = 3$. The error threshold and the captured energy percentage is set by practitioner to be $\varepsilon_{th} = 10^{-6}$ and $\gamma_{th} = 99.999\%$, respectively. It is evident that errors of the fixed-rank approximations $r = 2$ and $r = 3$ exceed the upper limit of the 10^{-6} , while the adaptive TDB maintain the error below the upper limit by increasing the rank to $r = 4$. The number of modes is later reduced to $r = 3$ as the dimensionality of the problem decreases for

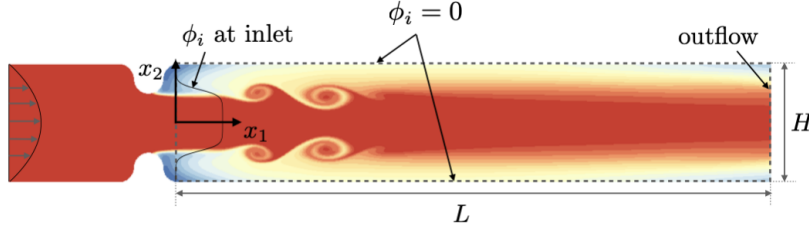


Figure 5: Incompressible turbulent reactive flow schematic.

the given γ_{th} . Figure 4(c) shows the singular values of the unfolded core tensor in the x_1 -direction for the fixed-rank and adaptive-rank cases as well as the corresponding HOSVD singular values, which are obtained by taking instantaneous SVD on the unfolded full-dimensional data. This shows that the fixed-rank and adaptive TDB decompositions closely follow the HOSVD.

3.2. Incompressible Turbulent Reactive Flow

In the second demonstration, we apply the TDB compression to a turbulent reactive flow. Turbulent reactive flows are multiscale and multivariate, whose high-fidelity numerical simulations result in massive datasets that with the current I/O restrictions of exascale simulations even storing the temporally resolved solution is becoming increasingly challenging let alone probing and analysis of the simulation data. This is particularly the case when a large number of species is involved. An example is the direct numerical simulation (DNS) of turbulent combustion, in which the creation of an ignition kernel – an intermittent phenomenon – occurs on the order of 10 simulation time steps, while typically every 400th time step is stored to maintain the I/O overhead at a reasonable level [5]. To demonstrate the application of TDB, we consider streaming data generated by a 2D advection-diffusion reaction problem:

$$\frac{\partial \phi_i}{\partial t} + (u \cdot \nabla) \phi_i = \nabla \cdot (\alpha_i \nabla \phi_i) + Q_i^S \quad (3.2)$$

where, ϕ_i is the concentration of i th reactant, α_i is the associated diffusion coefficient, Q_i^S denotes the nonlinear source that determines whether ϕ_i is produced or consumed and u is the velocity field of the flow. The reaction mechanisms model the blood coagulation cascade in a Newtonian fluid [43]. The simulation setup chosen in this work is identical to the case considered in reference [35]. Equation (3.2) is solved for $n_s = 23$ species and the velocity field is obtained by solving incompressible Navier-Stokes equations at $Re=1000$ using spectral element discretization. Equation (3.2) is advanced in time using fourth-order RK with $\Delta t = 5 \times 10^{-4}$. The numerical solution of Eq. (3.2) is cast as a streaming third-order tensor of size $N_1 \times N_2 \times N_3$, where $N_1 = 251$, $N_2 = 76$ and $N_3 = n_s = 23$ are the number of species.

We consider two different TDB compression schemes as follow:

$$\text{TDB-1:} \quad \phi(x_1, x_2, \eta, t) = \sum_{i_3=1}^{r_3} \sum_{i_2=1}^{r_2} \sum_{i_1=1}^{r_1} \mathbf{T}_{i_1 i_2 i_3}(t) u_{i_1}^{(1)}(x_1, t) u_{i_2}^{(2)}(x_2, t) u_{i_3}^{(3)}(\eta, t) \quad (3.3)$$

$$\text{TDB-2 (DBO):} \quad \phi(x_1, x_2, \eta, t) = \sum_{i_2=1}^{r_2} \sum_{i_1=1}^{r_1} \mathbf{T}_{i_1 i_2}(t) u_{i_1}^{(1)}(x_1, x_2, t) u_{i_2}^{(2)}(\eta, t), \quad (3.4)$$

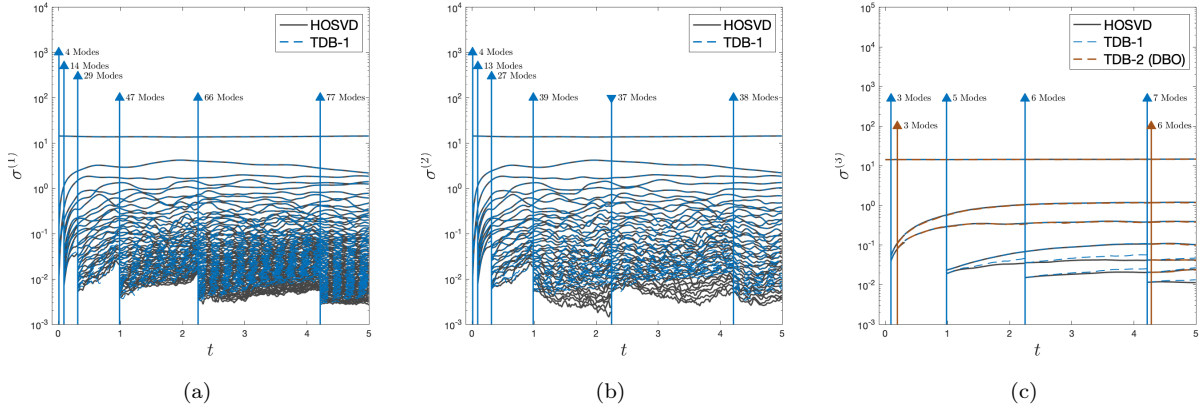


Figure 6: Compression of the 2D turbulent reactive flow. Singular values of the unfolded tensor in directions: (a) x_1 , (b) x_2 , and (c) η .

where the inner product in the physical and composition space are as follow:

$$\begin{aligned}
 \text{Physical space (TDB-1):} \quad & \langle u_{i_1}^{(1)}(x_1, t), u_{i_1'}^{(1)}(x_1, t) \rangle_{x_1} \simeq \mathbf{u}_{i_1}^{(1)T} \mathbf{W}^{(1)} \mathbf{u}_{i_1}^{(1)} \\
 & \langle u_{i_2}^{(2)}(x_2, t), u_{i_2'}^{(2)}(x_2, t) \rangle_{x_2} \simeq \mathbf{u}_{i_2}^{(2)T} \mathbf{W}^{(2)} \mathbf{u}_{i_2}^{(2)} \\
 \text{Physical space (TDB-2):} \quad & \langle u_{i_1}^{(1)}(\mathbf{x}, t), u_{i_1'}^{(1)}(\mathbf{x}, t) \rangle_{\mathbf{x}} \simeq \mathbf{u}_{i_1}^{(1)T} \mathbf{W}^{(1)} \mathbf{u}_{i_1}^{(1)} \\
 \text{Composition space (TDB-1):} \quad & \langle u_{i_3}^{(3)}(\eta, t), u_{i_3'}^{(3)}(\eta, t) \rangle_{\eta} \simeq \mathbf{u}_{i_3}^{(3)T} \mathbf{u}_{i_3}^{(3)} \\
 \text{Composition space (TDB-2):} \quad & \langle u_{i_2}^{(2)}(\eta, t), u_{i_2'}^{(2)}(\eta, t) \rangle_{\eta} \simeq \mathbf{u}_{i_2}^{(2)T} \mathbf{u}_{i_2}^{(2)}
 \end{aligned}$$

In TDB-1, $\mathbf{W}^{(1)}$ and $\mathbf{W}^{(2)}$ are quadrature weights obtained from spectral element discretizations of x_1 and x_2 directions, respectively. In TDB-2, $\mathbf{W}^{(1)}$ are the quadrature weights for 2D spectral element discretization i.e., both x_1 and x_2 directions. The inner product weight in the composition space for both schemes is the identity matrix. The above two schemes have different reduction errors and compression ratios. The main difference between the two decompositions is that in Eq. 3.3, the correlations between both spatial directions, i.e., x_1 , x_2 and the *composition* space, i.e., η are extracted, whereas in TDB-2, the correlation between x_1 and x_2 directions are not extracted. Both schemes are adaptive: modes are added and removed to keep the reconstruction error below $\varepsilon_{th} = 10^{-5}$ and the captured details above the $\gamma_{th} = 99.999\%$. TDB-2 was recently introduced in Ref. [35], where it was referred to as *dynamically bi-orthonormal* (DBO) decomposition since the species are decomposed to two sets of orthonormal modes in the spatial domain and the composition space. In the DBO formulation presented in Ref. [35], full-dimensional Eq. 3.2 is not solved; instead closed-form evolution equations for all three components of TDB-2 are derived, i.e., ODEs for $\underline{\mathbf{T}}_{i_1 i_2}(t)$ and $u_{i_2}^{(2)}(\eta, t)$ and PDEs for $u_{i_1}^{(1)}(x_1, x_2, t)$. We refer to DBO reduction in Ref. [35], as model-driven analogue of the data-driven reduction technique presented in this paper, because in the DBO formulation in Ref. [35] data generation is not required. In this section, we compare the model-driven DBO bases and the data-driven DBO bases that are the focus of this paper.

TDB-2 shows a slower error growth than TDB-1. To investigate this, in Figures 6(a)-6(c), we show the instantaneous singular values of the unfolded tensor in x_1 , x_2 and η directions for TDB-1 and TDB-2 as well as the instantaneous singular values obtained by performing HOSVD. Since in the TDB-2 decomposition, unfolding in x_1 and x_2 directions are not formed, in Figures 6(a)-6(b) only the singular values of TDB-1 and

HOSVD can be shown. It is clear that dominant singular values are captured accurately by both schemes. However, the effect of unresolved modes introduces a memory error. This error is driven by the energy of the unresolved modes and it affects the lower-energy modes more intensely than the higher-energy modes. If this error is left uncontrolled, it will eventually contaminate the higher-energy modes. The reconstruction error evolution for both schemes is shown in Figure 7(a). It is evident that the error grows at a much faster rate in TDB-1 compared to TDB-2. This can be explained by observing that the dimensionality in the spatial domain is often much higher than the dimensionality in the composition space. This means that in TDB-1, $\sigma^{(3)}(t)$ has a much faster decay rate compared to $\sigma^{(1)}(t)$ and $\sigma^{(2)}(t)$ as can be clearly seen in Figures 6(a)-6(c). In TDB-2, there is no reduction error in the x_1 or x_2 directions, and moreover, the turbulent reactive flow shows a very low-dimensional dynamics in the composition space (η), as a result the overall energy of the unresolved modes is much smaller, which in turn leads to a slower error growth rate. This also means that in an adaptive mode, one has to do calculate HOSVD more often in TDB-1 than in TDB-2.

In Figure 8, we compare the reconstructed data for the eighth species at five time instants. The reconstructed data are in good agreement with DNS snapshots, however, the form of error is different. The error is computed as the absolute value of the difference between the DNS and reconstructed TDB data. The resulting error from TDB-1 appears to have much finer structure than that of TDB-2. That is because in TDB-1, the unresolved subspaces in each of the x_1 and x_2 dimensions have very fine structures and they dominate the error, whereas in TDB-2 the error is due to the unresolved subspace in the η direction. The TDB-1 error at $t = 1, 2, 3, 4$ is less than TDB-2, mainly because of frequent HOSVD reinitialization in the adaptivity process. However, the maximum error of TDB-1 is larger than that of TDB-2. For better comparison, the error color bar is set from 0 to 0.5, while the maximum errors for TDB-1 and TDB-2 are 0.14 and 0.4, respectively.

TDB-1 and TDB-2 have different storage costs for the same reconstruction errors. In TDB-2, slower error growth rate comes at the cost of storing r two-dimensional bases with the storage cost of rN_1N_2 as opposed to TDB-1, where the storage cost of the spatial bases is $r_1N_1 + r_2N_2$. The overall storage cost of TDB-1 is: $S_{TDB-1} = r_1N_1 + r_2N_2 + r_3n_s + r_1r_2r_3$ and the storage cost of TDB-2 is: $S_{TDB-2} = rN_1N_2 + rn_s + r^2$. The comparison of the storage cost of TDB-1 and TDB-2 for the same reconstruction error depends on the values of r_1 and r_2 . These two storage costs for the same number of modes in the composition space, i.e., $r = r_3 = 7$ are shown in Figure 7(b). If r_1 and r_2 are large enough, the storage cost of TDB-1 exceeds that of TDB-2. In our study, the weighted compression ratio are $\overline{CR}_{TDB-1} = 15.62$ and $\overline{CR}_{TDB-2} = 6.6$ where the total size of data $35GB$ compressed to $2.2GB$ and $5.3GB$ by TDB-1 and TDB-2, respectively.

In the DBO formulation presented in Ref. [35], a coupled set of PDEs for the 2D bases and ODEs for the low-rank matrices are solved without using any data. The goal of the model-driven DBO [35] is to reduce the computational cost and memory requirement of solving species transport equations as well as reducing the I/O load. In this work, our goal is to compress the streaming data generated by the full-dimensional model. In Figure 9, the first and second most dominant modes of model-driven and data-driven DBOs for different instances of times are shown. It is clear that the bases for both model-driven DBO and data-driven DBO are nearly identical.

3.3. Stochastic Turbulent Reactive Flow

Quantifying uncertainties of transport and chemistry model parameters has major implications for the field of chemically reactive flows. An uncertainty quantification (UQ) analysis can significantly reduce the experimental costs by effectively allocating limited resources on reducing the uncertainty of key parameters, and inform mechanism reduction by determining the least important parameters or detecting reaction pathways that are unimportant and can be eliminated [44–46]. Any sampling-based technique, e.g., Monte Carlo or probabilistic collocation methods (PCM) for UQ analysis of this problem can generate very large datasets. In this demonstration, we show how TDB can be utilized to extract correlation between different random samples in addition to the multidimensional correlations presented in the previous example, to reduce the

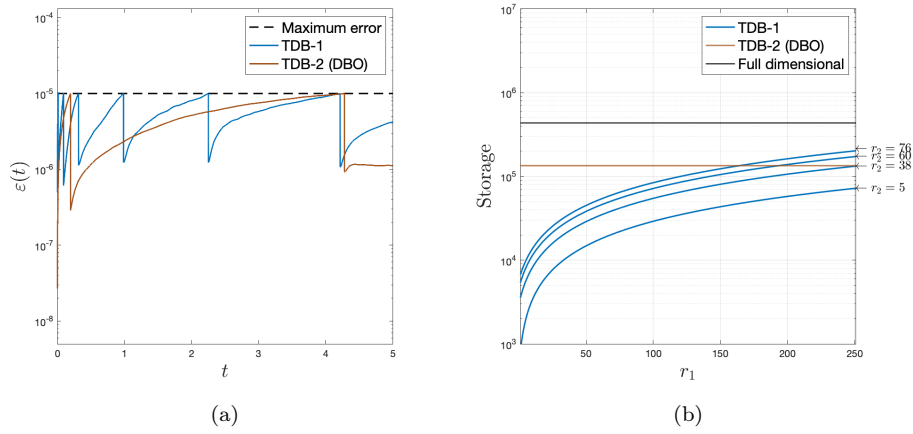


Figure 7: Compression of turbulent reactive flow data using TDB-1 and TDB-2 (DBO) schemes: (a) error evolution, (b) storage cost.

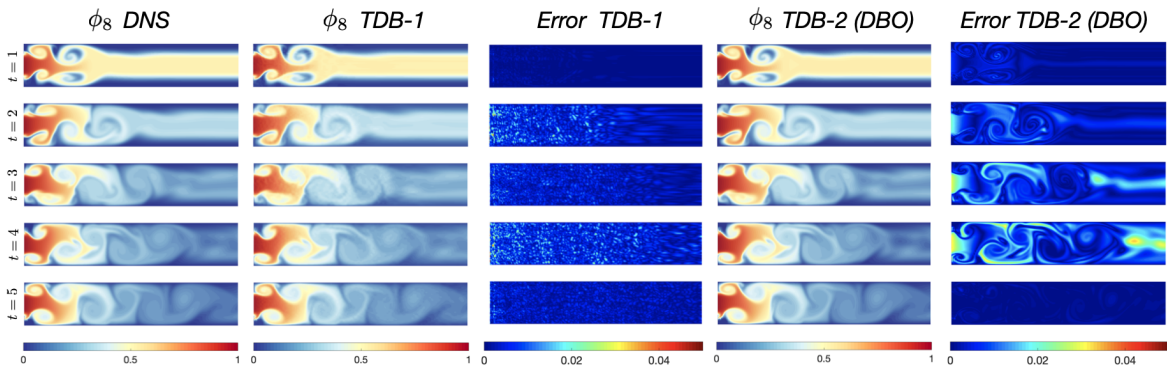


Figure 8: Unsteady reactive flow: Comparison between DNS and TDB reconstructed species concentration.

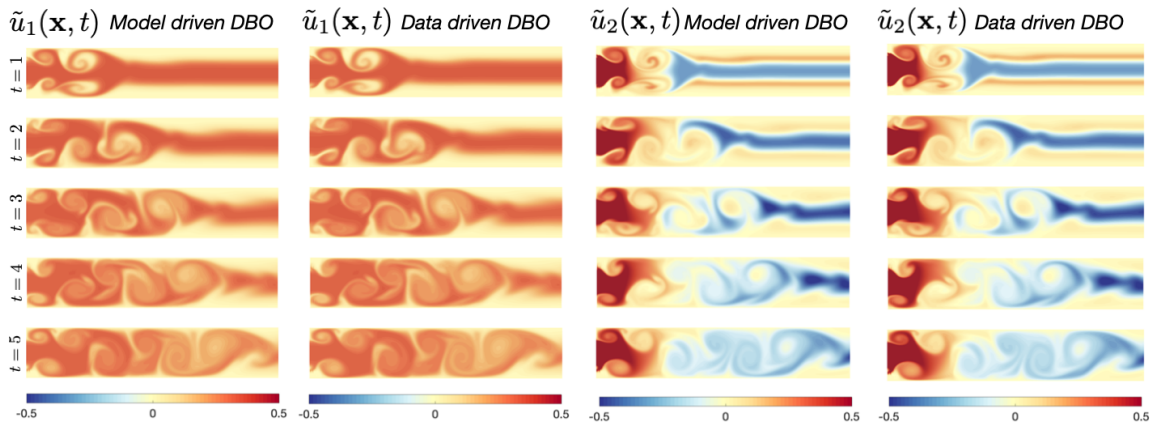


Figure 9: Turbulent reactive flow: Comparison between the first two dominant modes of the model-driven and data-driven DBO.

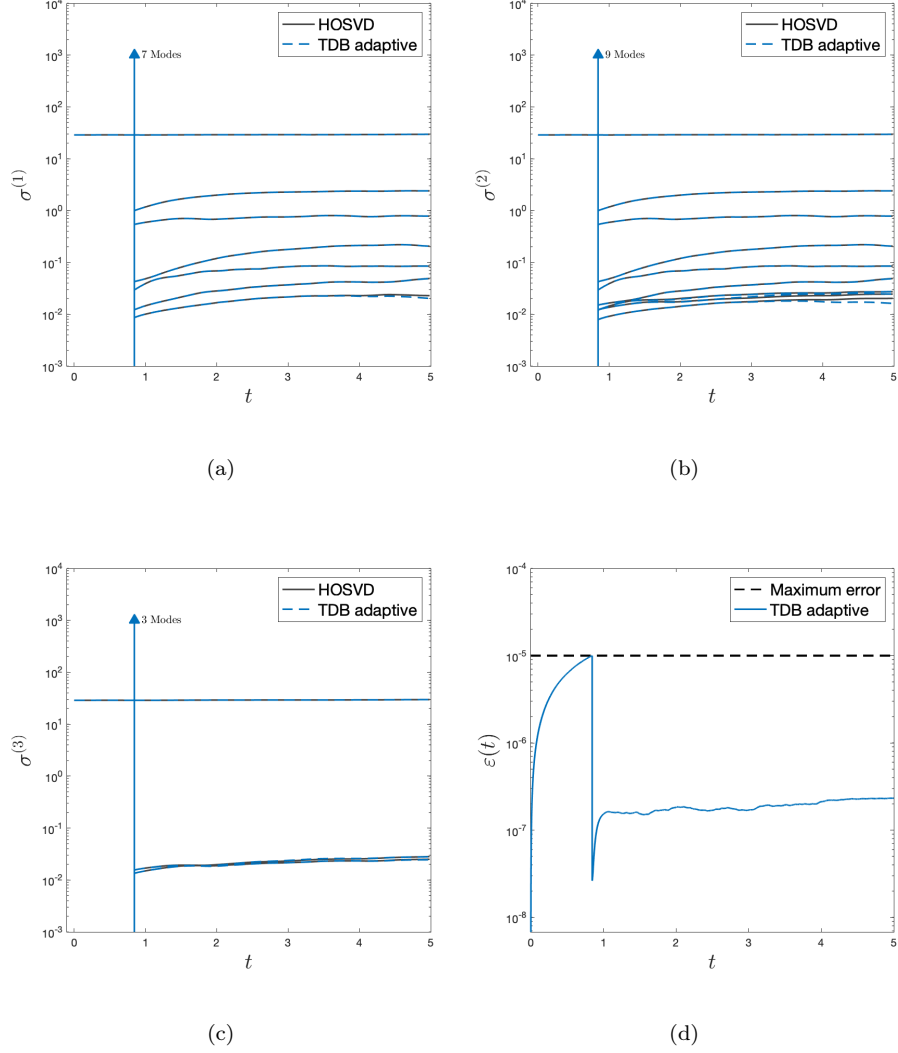


Figure 10: Incompressible turbulent reactive flow uncertainty quantification. Singular values of the unfolded tensor in: (a) x_1 , (b) x_2 , (c) η , and (d) error evolution.

storage cost of the data generated. In this section, we study the compression of resulting data from incompressible reactive flow with random diffusion coefficients. We consider the problem of uncertainty diffusion coefficients for two species (α_1 and α_4) in Eq. 3.2. We assume both of these two coefficients are independent random variables as in the following:

$$\boldsymbol{\xi} = [\xi_1, \xi_2] = (1 + 0.05\omega)[\alpha_1, \alpha_4],$$

where ω is a uniform random variable $\sim \mathcal{U}[-1, 1]$. The rest of the problem setup remains identical to the problem considered in §3.2. We consider a collocation grid of size $s = 4 \times 4$ in the random space, which requires 16 forward DNS simulations. We consider the following TDB compression scheme:

$$\phi(\mathbf{x}, \eta, \boldsymbol{\xi}, t) = \sum_{i_3=1}^{r_3} \sum_{i_2=1}^{r_2} \sum_{i_1=1}^{r_1} \mathbf{T}_{i_1 i_2 i_3}(t) u_{i_1}^{(1)}(x_1, x_2, t) u_{i_2}^{(2)}(\eta, t) u_{i_3}^{(3)}(\xi_1, \xi_2, t). \quad (3.5)$$

The rationale for choosing a 2D TDB for the random space rather than two 1D TDBs is that the cost of storing 2D random bases is negligible. On the other hand, choosing two 1D random TDBs would have increased the order of the core tensor from 3 to 4. Another valid choice for TDB is to combine the composition space and the random direction into a 3D space. However, the interpretability of 1D TDB in the composition space is quite appealing. The $u_{i_2}^{(2)}(\eta, t)$'s represent a time-dependent subspace in the composition space. In which the inner product in the random space is defined as follow:

$$\langle u_{i_3}^{(3)}(\xi_1, \xi_2, t), u_{i_3'}^{(3)}(\xi_1, \xi_2, t) \rangle_{\boldsymbol{\xi}} = \mathbb{E}[u_{i_3}^{(3)}(\xi_1, \xi_2, t) u_{i_3'}^{(3)}(\xi_1, \xi_2, t)] \simeq \mathbf{u}_{i_3}^{(3)T} \mathbf{W}^{(3)} \mathbf{u}_{i_3}^{(3)},$$

where $\mathbf{W}^{(3)}$ is the probabilistic collocation weight. Each random TDB in the discrete form is represented by a vector of size s , i.e., $\mathbf{u}_i^{(3)} \in \mathbb{R}^{s \times 1}$. Different sampling schemes might be used here. For example, one can use Monte Carlo samples. In that case, the inner product weight would be a diagonal matrix with all diagonal entries equal to $1/s$.

Since there is a high degree of correlation between random samples of species fields, the TDB compression can achieve the high compression ratio $\overline{CR} = 42.75$ compared to the previous cases and compress the size of data from $561.5GB$ to $13.1GB$. To examine this, we show the resulting singular values of the unfolded core tensor and compare them with HOSVD singular values in Figures 10(a)-10(c). Based on these figures, we make the following observations: (i) the dominant singular values are captured accurately; (ii) similar to TDB-2 the singular values decay rate is fast for this compression scheme compared to TDB-1; (iii) the problem dimension does not change after $t = 1$, and therefore, the number of modes remains the same; (iv) the random space has the lowest dimensionality, which means the generated data are highly correlated with respect to the random diffusion coefficients. Figure 10(d) shows the reconstruction error evolution in which it exceeds the maximum limit around $t = 1$ due to the increase in dimensionality. Using the reinitialization and mode adjustment in each direction with respect to the defined $\gamma_{th} = 99.999\%$ the error decreases. Since after $t = 1$ the dimensionality does not change, the error remains the same.

3.4. Three-dimensional Turbulent Channel Flow

In the last demonstration case, we use TDB to compress the data obtained by the direct numerical simulation (DNS) of turbulent channel flow. The data are generated by the finite difference solver in Ref. [47]. The Reynolds number based on the friction velocity is $Re_\tau = 180$. The length, width and height of the channel are π , 2π , and 2, respectively. The number of grid points in all dimensions is 150 with uniform distribution in streamwise and spanwise directions. The grid is clustered near the channel wall in the wall-normal direction. We apply TDB to the streamwise velocity component as compression of other field variables result in the same qualitative observations. We consider one-dimensional TDBs as follows:

$$v(x_1, x_2, x_3, t) = \sum_{i_3=1}^{r_3} \sum_{i_2=1}^{r_2} \sum_{i_1=1}^{r_1} \mathbf{T}_{i_1 i_2 i_3}(t) u_{i_1}^{(1)}(x_1, t) u_{i_2}^{(2)}(x_2, t) u_{i_3}^{(3)}(x_3, t). \quad (3.6)$$

The TDB equations are evolved with the time step of $\Delta t = 10^{-3}$, which is the same as the Δt used in the DNS time integration. We consider two cases with different error thresholds. Case-I with the $\gamma_{th} = 99.9999\%$ and Case-II with the $\gamma_{th} = 99.999\%$. For both cases the error threshold is set to be $\varepsilon_{th} = 3.3 \times 10^{-5}$. In Case-I, the initial value of the multirank is $(r_1, r_2, r_3) = (68, 81, 50)$ and in Case-II the initial multirank is $(r_1, r_2, r_3) = (54, 57, 36)$. The error evolution for both case are shown in Figure 11(a). The compression ratios for Case-I and Case-II are $\overline{CR} = 9.62$ and $\overline{CR} = 26.90$, respectively. For this problem, performing HOSVD at different time instants result in the same multirank and that is because the flow is statistically steady state, and therefore, the rank of the systems does not change in time. However, in the TDB formulation, the error still grows because of the effect of the unresolved subspace. This error is controlled by the adaptive scheme. The error evolution for both cases are shown in Figure 11(a). In Case-II, since the unresolved space has larger energy, the error grows with faster rate compared to Case-I. As a result, in Case-II, 9 HOSVD initializations are performed as opposed to one initialization in Case-I. Figure 11(b) shows the singular values

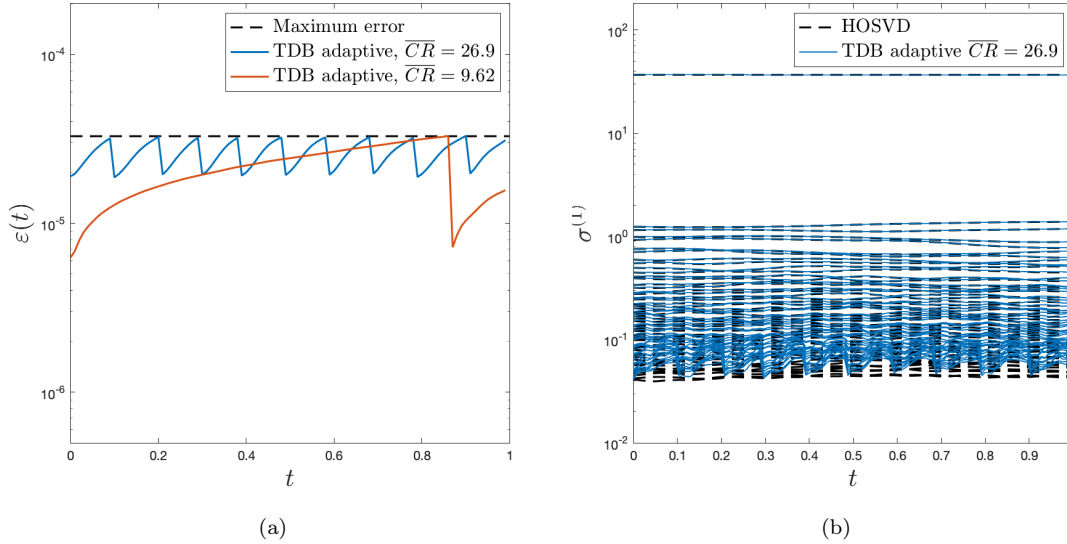


Figure 11: Turbulent channel flow: (a) Error evolution. (b) Singular values of the unfolded tensor in x_1 direction.

of the unfolded TDB core tensor along the x_1 direction against that of the full-dimensional data obtained by HOSVD. There is a large gap between the first singular value and the rest of the singular values. We also observe that the low-energy modes values are more contaminated by the error induced by the unresolved subspace.

Figures 12(a) and 12(b) compare the *RMS* and mean velocity at $t = 1$ from TDB reconstructed calculations with Ref. [47] and HOSVD reconstruction. In these figures, the TDB and HOSVD reconstructed *RMS* and the mean velocity are in good agreement, however; due to unresolved modes the reconstructed data has discrepancy compared to the DNS results. We can observe the higher compression ratio is causing more discrepancy due to more unresolved modes. Figures 12(c) to 12(e) compare the TDB and HOSVD reconstructed data with the streamed data for the case with high compression ratio at $t = 1$ in 3D format. Based on these figures, we can conclude that both the HOSVD and TDB reconstruction are in good agreement with the original data.

4. Summary

We present an in situ compression method based on TDB, in which the multidimensional streaming data are decomposed into a set of TDB and a time-dependent core tensor. We derived closed-form evolution equations for the TDB and the core tensor. The presented methodology is adaptive and maintains the error below the defined threshold ε_{th} by adding/removing ranks. The computational cost of solving TDB computational complexity scales linearly with the data size, making it suitable for large-scale streaming datasets.

We perform this compression method on four cases:

1. Runge Function: Where we demonstrated the adaptive mode addition/removal. We also investigated the effect of different time integration schemes on the compression error of TDB.
2. Incompressible Turbulent Reactive Flow: In this case, we compress the data by two TDB schemes (TDB-1 and TDB-2). TDB-1 has a higher compression ratio ($\overline{CR} = 15.62$, which compresses $35GB$ to $2.2GB$) since it can decompose the physical space more than TDB-2 using one dimensional basis. TDB-2 scheme has a lower compression ratio ($\overline{CR} = 6.6$, which compresses $35GB$ to $5.3GB$) because it uses a two dimensional basis for physical space. Since the physical space has a high dimensionality compared

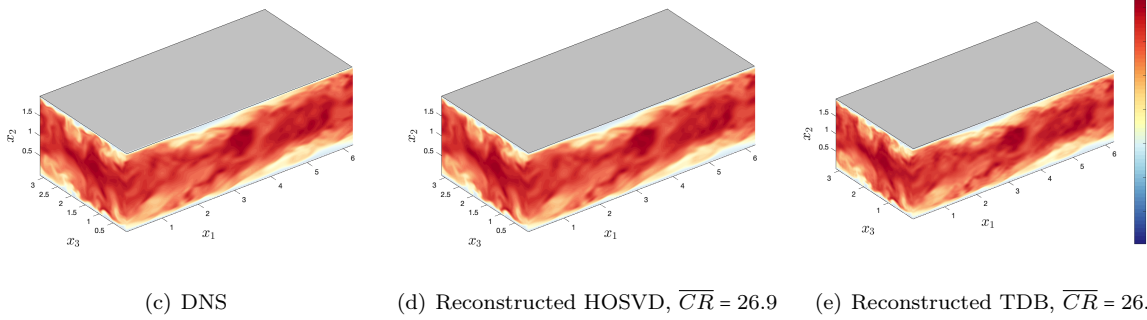
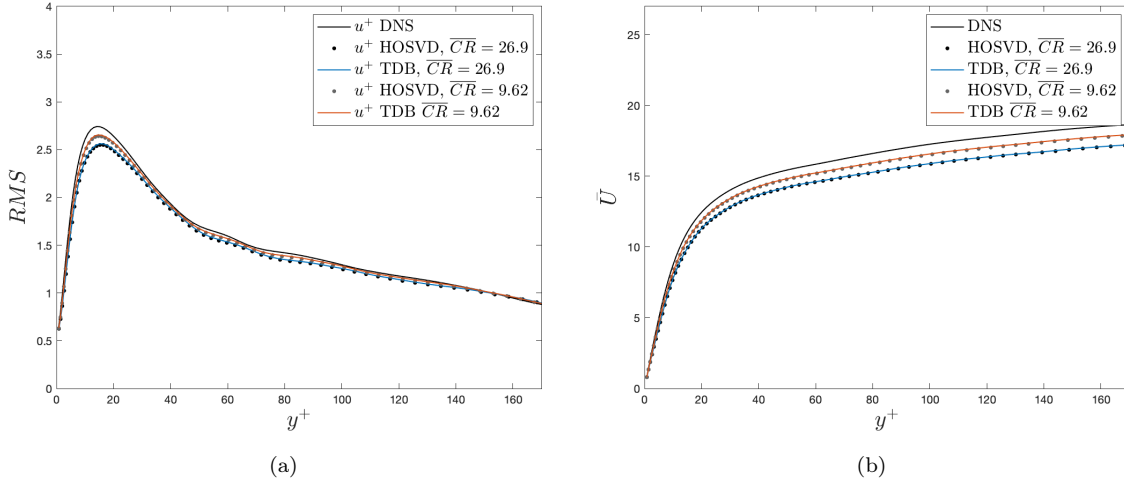


Figure 12: Turbulent channel flow: (a) RMS, (b) mean profiles comparison between DNS and the same-rank HOSVD and TDB reductions. Comparison of DNS and the same-rank HOSVD and TDB reductions: (c) DNS, (d) reconstructed TDB, and (e) reconstructed HOSVD.

to composition space, the error growth rate for TDB-1 is higher and requires frequent reinitialization and mode adjustments.

3. Incompressible Turbulent Reactive Flow with Random Diffusion Coefficient: This problem is the same as the second case with sixteen samples random diffusion coefficients. The TDB scheme in this problem is similar to the TDB-2 with an additional two dimensional basis for the random space. Since the TDB can exploit more correlation in the streamed data, the compression ratio is higher than the previous cases ($\overline{CR} = 42.75$, which compresses $561.5GB$ to $13.1GB$).
4. Three-dimensional Turbulent Channel Flow: In this problem, we compare two different compression ratios. We observed that the TDB with higher compression ratio has a slower growth rate compared to the TDB with lower compression ratio. For both cases, the TDB reconstructed results are in good agreement with HOSVD.

The current methodology only exploits multidimensional correlation in all dimensions except the temporal direction. For the future studies, we will extend this methodology to exploit temporal correlations. We will also pursue building real-time reduced order models for diagnostic and predictive purposes.

Acknowledgements

This project was supported by an award by Air Force Office of Scientific Research (PM: Dr. Fariba Fahroo) award FA9550-21-1-0247 and support from NASA’s Transformational Tools and Technologies Project (Cooperative Agreement No. 80NSSC18M0150).

References

- [1] J. Slotnick, A. Khodadoust, J. Alonso, D. Darmofal, W. Gropp, E. Lurie, and D. Mavriplis, “CFD vision 2030 study: a path to revolutionary computational aerosciences,” *National Aeronautics and Space Administration, Langley Research Center*, 2014.
- [2] E. P. Duque, S. T. Imlay, S. Ahern, C. Guoning, and D. L. Kao, “Nasa cfd vision 2030 visualization and knowledge extraction: Panel summary from aiaa aviation 2015 conference,” in *54th AIAA Aerospace Sciences Meeting*, p. 1927, 2016.
- [3] J. Dongarra, J. Hittinger, J. Bell, L. Chacon, R. Falgout, M. Heroux, P. Hovland, E. Ng, C. Webster, and S. Wild, “Applied mathematics research for exascale computing,” tech. rep., Lawrence Livermore National Lab.(LLNL), Livermore, CA (United States), 2014.
- [4] “Data reduction for science,” *Report of the DOE Workshop on Brochure from Advanced Scientific Computing Research Workshop*, 2021.
- [5] J. C. Bennett, H. Abbasi, P. Bremer, R. Grout, A. Gyulassy, T. Jin, S. Klasky, H. Kolla, M. Parashar, V. Pascucci, P. Pebay, D. Thompson, H. Yu, F. Zhang, and J. Chen, “Combining in-situ and in-transit processing to enable extreme-scale scientific analysis,” in *SC ’12: Proceedings of the International Conference on High Performance Computing, Networking, Storage and Analysis*, pp. 1–9, 2012.
- [6] S. W. Son, Z. Chen, W. Hendrix, A. Agrawal, W.-k. Liao, and A. Choudhary, “Data compression for the exascale computing era-survey,” *Supercomputing frontiers and innovations*, vol. 1, no. 2, pp. 76–88, 2014.
- [7] S. Li, N. Marsaglia, C. Garth, J. Woodring, J. Clyne, and H. Childs, “Data reduction techniques for simulation, visualization and data analysis,” in *Computer Graphics Forum*, vol. 37, pp. 422–447, Wiley Online Library, 2018.
- [8] P. Lindstrom and M. Isenburg, “Fast and efficient compression of floating-point data,” *IEEE transactions on visualization and computer graphics*, vol. 12, no. 5, pp. 1245–1250, 2006.
- [9] N. Fout and K.-L. Ma, “An adaptive prediction-based approach to lossless compression of floating-point volume data,” *IEEE Transactions on Visualization and Computer Graphics*, vol. 18, no. 12, pp. 2295–2304, 2012.
- [10] H. Cheng, Z. Gimbutas, P.-G. Martinsson, and V. Rokhlin, “On the compression of low rank matrices,” *SIAM Journal on Scientific Computing*, vol. 26, no. 4, pp. 1389–1404, 2005.
- [11] A. M. Dunton, L. Jofre, G. Iaccarino, and A. Doostan, “Pass-efficient methods for compression of high-dimensional turbulent flow data,” *Journal of Computational Physics*, vol. 423, p. 109704, 2020.
- [12] C. W. Therrien, *Discrete random signals and statistical signal processing*. Prentice Hall PTR, 1992.
- [13] J. A. Tropp, A. Yurtsever, M. Udell, and V. Cevher, “Practical sketching algorithms for low-rank matrix approximation,” *SIAM Journal on Matrix Analysis and Applications*, vol. 38, no. 4, pp. 1454–1485, 2017.
- [14] H. Kolla, K. Aditya, and J. H. Chen, *Higher Order Tensors for DNS Data Analysis and Compression*, pp. 109–134. Cham: Springer International Publishing, 2020.

- [15] G. Zhou, A. Cichocki, and S. Xie, “Decomposition of big tensors with low multilinear rank,” 2014.
- [16] K. T. Carlberg, A. Jameson, M. J. Kochenderfer, J. Morton, L. Peng, and F. D. Witherden, “Recovering missing cfd data for high-order discretizations using deep neural networks and dynamics learning,” *Journal of Computational Physics*, vol. 395, pp. 105–124, 2019.
- [17] A. Glaws, R. King, and M. Sprague, “Deep learning for in situ data compression of large turbulent flow simulations,” *Physical Review Fluids*, vol. 5, no. 11, p. 114602, 2020.
- [18] Y. Liu, Y. Wang, L. Deng, F. Wang, F. Liu, Y. Lu, and S. Li, “A novel in situ compression method for cfd data based on generative adversarial network,” *Journal of Visualization*, vol. 22, no. 1, pp. 95–108, 2019.
- [19] Z. Gong, T. Rogers, J. Jenkins, H. Kolla, S. Ethier, J. Chen, R. Ross, S. Klasky, and N. F. Samatova, “Mloc: Multi-level layout optimization framework for compressed scientific data exploration with heterogeneous access patterns,” in *2012 41st International Conference on Parallel Processing*, pp. 239–248, IEEE, 2012.
- [20] T. P. Sapsis and P. F. Lermusiaux, “Dynamically orthogonal field equations for continuous stochastic dynamical systems,” *Physica D: Nonlinear Phenomena*, vol. 238, no. 23-24, pp. 2347–2360, 2009.
- [21] M. Cheng, T. Y. Hou, and Z. Zhang, “A dynamically bi-orthogonal method for time-dependent stochastic partial differential equations i: Derivation and algorithms,” *Journal of Computational Physics*, vol. 242, pp. 843–868, 2013.
- [22] M. Choi, T. P. Sapsis, and G. E. Karniadakis, “On the equivalence of dynamically orthogonal and bi-orthogonal methods: Theory and numerical simulations,” *Journal of Computational Physics*, vol. 270, pp. 1 – 20, 2014.
- [23] E. Musharbash and F. Nobile, “Dual dynamically orthogonal approximation of incompressible Navier-Stokes equations with random boundary conditions,” *Journal of Computational Physics*, vol. 354, pp. 135–162, 2018.
- [24] H. Babaee, “An observation-driven time-dependent basis for a reduced description of transient stochastic systems,” *Proceedings of the Royal Society A: Mathematical, Physical and Engineering Sciences*, vol. 475, no. 2231, p. 20190506, 2019.
- [25] P. Patil and H. Babaee, “Real-time reduced-order modeling of stochastic partial differential equations via time-dependent subspaces,” *Journal of Computational Physics*, vol. 415, p. 109511, 2020.
- [26] H. Babaee and T. Sapsis, “A minimization principle for the description of modes associated with finite-time instabilities,” *Proceedings of the Royal Society A: Mathematical, Physical and Engineering Sciences*, vol. 472, no. 2186, p. 20150779, 2016.
- [27] A. Blanchard, S. Mowlavi, and T. Sapsis, “Control of linear instabilities by dynamically consistent order reduction on optimally time-dependent modes,” *Nonlinear Dynamics*, vol. In press, 2018.
- [28] M. Donello, M. Carpenter, and H. Babaee, “Computing sensitivities in evolutionary systems: A real-time reduced order modeling strategy,” *arXiv preprint arXiv:2012.14028*, 2020.
- [29] A. G. Nouri, H. Babaee, P. Givi, H. K. Chelliah, and D. Livescu, “Skeletal model reduction with forced optimally time dependent modes,” *Combustion and Flame*, p. 111684, 2021.
- [30] M. H. Beck, A. Jäckle, G. A. Worth, and H. D. Meyer, “The multiconfiguration time-dependent Hartree (MCTDH) method: a highly efficient algorithm for propagating wavepackets,” *Physics Reports*, vol. 324, pp. 1–105, 1 2000.

- [31] C. Bardos, F. Golse, A. D. Gottlieb, and N. J. Mauser, “Mean field dynamics of fermions and the time-dependent Hartree–Fock equation,” *Journal de Mathématiques Pures et Appliquées*, vol. 82, no. 6, pp. 665–683, 2003.
- [32] O. Koch and C. Lubich, “Dynamical tensor approximation,” *SIAM Journal on Matrix Analysis and Applications*, vol. 31, pp. 2360–2375, 2017/04/02 2010.
- [33] A. Dektor and D. Venturi, “Dynamically orthogonal tensor methods for high-dimensional nonlinear pdes,” *Journal of Computational Physics*, vol. 404, p. 109125, 2020.
- [34] T. G. Kolda and B. W. Bader, “Tensor decompositions and applications,” *SIAM Review*, vol. 51, no. 3, pp. 455–500, 2009.
- [35] D. Ramezani, A. G. Nouri, and H. Babae, “On-the-fly reduced order modeling of passive and reactive species via time-dependent manifolds,” *Computer Methods in Applied Mechanics and Engineering*, vol. 382, p. 113882, 2021.
- [36] T. Sapsis and P. Lermusiaux, “Dynamically orthogonal field equations for continuous stochastic dynamical systems,” *Physica D: Nonlinear Phenomena*, vol. 238, no. 23–24, pp. 2347–2360, 2009.
- [37] H. Babae and T. P. Sapsis, “A minimization principle for the description of modes associated with finite-time instabilities,” *Proceedings of the Royal Society of London A: Mathematical, Physical and Engineering Sciences*, vol. 472, no. 2186, 2016.
- [38] M. Cheng, T. Y. Hou, and Z. Zhang, “A dynamically bi-orthogonal method for time-dependent stochastic partial differential equations i: Derivation and algorithms,” *Journal of Computational Physics*, vol. 242, no. 0, pp. 843 – 868, 2013.
- [39] H. Babae, M. Farazmand, G. Haller, and T. P. Sapsis, “Reduced-order description of transient instabilities and computation of finite-time Lyapunov exponents,” *Chaos: An Interdisciplinary Journal of Nonlinear Science*, vol. 27, p. 063103, 06 2017.
- [40] A. J. Chorin, O. H. Hald, and R. Kupferman, “Optimal prediction and the mori–zwanzig representation of irreversible processes,” *Proceedings of the National Academy of Sciences*, vol. 97, no. 7, pp. 2968–2973, 2000.
- [41] T. Liu, J. Wang, Q. Liu, S. Alibhai, T. Lu, and X. He, “High-ratio lossy compression: Exploring the autoencoder to compress scientific data,” *IEEE Transactions on Big Data*, 2021.
- [42] D. Mishra, S. K. Singh, and R. K. Singh, “Wavelet-based deep auto encoder-decoder (wdaed)-based image compression,” *IEEE Transactions on Circuits and Systems for Video Technology*, vol. 31, no. 4, pp. 1452–1462, 2020.
- [43] Z. Li, A. Yazdani, A. Tartakovsky, and G. E. Karniadakis, “Transport dissipative particle dynamics model for mesoscopic advection-diffusion-reaction problems,” *The Journal of Chemical Physics*, vol. 143, p. 014101, 2020/07/13 2015.
- [44] K. Braman, T. A. Oliver, and V. Raman, “Adjoint-based sensitivity analysis of flames,” *Combustion Theory and Modelling*, vol. 19, pp. 29–56, 01 2015.
- [45] M. Lemke, L. Cai, J. Reiss, H. Pitsch, and J. Sesterhenn, “Adjoint-based sensitivity analysis of quantities of interest of complex combustion models,” *Combustion Theory and Modelling*, vol. 23, pp. 180–196, 01 2019.
- [46] R. Langer, J. Lotz, L. Cai, F. vom Lehn, K. Leppkes, U. Naumann, and H. Pitsch, “Adjoint sensitivity analysis of kinetic, thermochemical, and transport data of nitrogen and ammonia chemistry,” *Proceedings of the Combustion Institute*, 2020.

- [47] V. Vuorinen and K. Keskinen, “Dnslab: A gateway to turbulent flow simulation in matlab,” *Computer Physics Communications*, vol. 203, pp. 278–289, 2016.